

## **Particle Shadow Velocimetry (PSV) in bubbly flows**

Heßenkemper, H.; Ziegenhein, T.;

Originally published:

April 2018

**International Journal of Multiphase Flow 106(2018), 268-279**

DOI: <https://doi.org/10.1016/j.ijmultiphaseflow.2018.04.015>

Perma-Link to Publication Repository of HZDR:

<https://www.hzdr.de/publications/Publ-26515>

Release of the secondary publication  
on the basis of the German Copyright Law § 38 Section 4.

CC BY-NC-ND

# Particle Shadow Velocimetry (PSV) in bubbly flows

H. Hessenkemper\*, T. Ziegenhein

Helmholtz-Zentrum Dresden-Rossendorf e.V., 01314 Dresden, Germany

\* Corresponding author. Tel.: +49 3512602620; fax: +49 3512603440.

E-mail address: [h.hessenkemper@hzdr.de](mailto:h.hessenkemper@hzdr.de) (Hendrik Hessenkemper)

## Abstract

The interaction of gas bubbles and the surrounding liquid in bubbly flows is a complex hydrodynamic phenomenon. Precise measurements of the liquid velocity are mandatory to generate accurate models and CFD-validation data sets. For this purpose, methods for Particle Shadow Velocimetry (PSV) that are using a volume illumination and a small depth of field (DOF) are developed in the presented work. Experiments with an oscillating plume were conducted in a rectangular bubble column to test the PSV methods. The results obtained with a Particle Image Velocimetry (PIV) and a Particle Tracking Velocimetry (PTV) processing procedure agree very well with respect to velocity profiles and turbulence parameters. As discussed in previous work, PSV methods have a much simpler experimental setup and can handle much higher gas fractions. With the present findings, robust PSV algorithms for PIV and PTV in bubbly flows are now available.

**Keywords.** Particle Shadow Velocimetry, Multiphase Flow, Bubbly flow, Particle Image Velocimetry, Particle Tracking Velocimetry

# 1. Introduction

---

Bubbly flows occur in several industrial applications, in particular in chemical and biological reactors, wastewater treatment and nuclear plants. To develop meaningful models of the liquid flow behavior, reliable measurements of the liquid velocity are of great importance since rising bubbles accelerate the flow and induce turbulence. With tracer particles added to the flow and a proper handling of the bubble interface, Particle Image Velocimetry (PIV) or Particle Tracking Velocimetry (PTV) can be used for such measurements (Ziegenhein, et al., 2016) , (Bröder & Sommerfeld, 2007).

By using PIV, the movement of the flow is determined via correlating the particle displacement in small subareas, so-called interrogation areas, of two delayed image recordings (Raffel, et al., 1998). In contrast to PIV, PTV identifies and tracks single particles from one image to another. An advantage of PTV is that two or three times higher spatial resolution can be theoretical achieved as Marxen et al. 2000 demonstrated. The drawback however, are problems with identifying particles and matching pairs correctly at high particle densities. In bubbly flows, PTV has some advantages since particle motions close to a bubble can be tracked, whereas PIV velocity determinations are limited due to the disturbing influence of the bubble surface in the image area (Murai, et al., 2006).

In conventional PIV and PTV measurements, the particles are illuminated with a laser sheet from the side, which causes problems in bubbly flows due to the presence of the gas phase. In particular, light scattering and reflection at the bubble surfaces disturb the measurement and prevent displacement determinations close to the surfaces. Moreover, bubbles throw shadows in which no velocity measurements are possible. Even by using fluorescing particles and applying appropriate filters the usability of laser-based PIV and PTV is limited for higher gas fractions (Brücker, 2000).

A possible alternative to overcome these problems is the so-called Particle Shadow Velocimetry (PSV) method. With PSV, the measurement of the liquid velocity is possible but without laser-systems for illuminating the tracer particles. For the PSV method, the region of interest is backlight illuminated with standard LEDs or halogen lamps, whereby scattering effects are strongly reduced and no lateral bubble shadows occur. By using a small depth of field (DOF), particles in a thin area of the volume can be identified so that the particle displacement is evaluated in a quasi-2D measuring volume (Estevadeordal & Goss, 2005).

Although this method is not distributed widely in the community, several relevant use cases can be found in the literature. Santiago et al. 1998 determined 2D velocity fields with volume illumination and a small DOF. They used fluorescing particles for their  $\mu$ PIV measurements in micro fluidic devices. An advantage is that adjusting and aligning a very thin light sheet is very challenging in comparison to adjust a narrow DOF. Therefore, backlight illuminating became quite popular for  $\mu$ PIV measurements over the last decades (Wereley & Meinhart, 2010).

Estevadeordal & Goss 2005 introduced the term Particle Shadow Velocimetry for velocity measurements using only the casted shadow of the particles. In their work, they

carried out several test measurements in single phase flows with the PSV method and demonstrated the concept feasibility and validity.

Khodaparast et al. 2014 used  $\mu$ PSV to measure two-phase flow velocities in microchannels. In their setup liquid-liquid and liquid-gas flows were investigated. The  $\mu$ PSV technique allowed them to simultaneously determine dispersed phase properties like droplet/bubble size and shape, as well as the determination of velocity fields in the continuous and the dispersed phase.

To the authors knowledge the present work is the first to test the PSV technique in larger scale two-phase flows like bubbly flows in a bubble column. For this purpose, liquid velocity fields induced by an oscillating plume with changing gas flow rates and gas fractions up to 15% are investigated in a rectangular bubble column. The corresponding experimental setup is described in the next section. Two processing procedures for the displacement determination of sharp particle shadows are introduced afterwards. The first is based on PIV evaluation steps and the second on PTV evaluation steps for high particle densities. Both procedures were developed in the framework of an in-house software package, which is based on the programming language Java™. Since PIV and PTV are commonly referred to measurements with laser- or LED-sheets coming from the side, the velocity determination with PIV using particle shadows will be denoted as Particle Shadow Image Velocimetry (PSIV) and with PTV as Particle Shadow Tracking Velocimetry (PSTV) to prevent confusion. Finally, averaged velocity profiles as well as basic turbulence parameters are discussed and compared for both procedures.

## 2. Experimental setup

---

The used bubble column is 50 mm deep, 250 mm width and is filled with deionized water to a height of 800 mm. Air is injected through eight spargers with an inner diameter of 1.5 mm, inserted at the bottom plate. The PSV measurements are executed at a height of 200 mm for a gas flowrate of 3 l/min, 5 l/min, 7 l/min and 13 l/min. A sketch of the experimental setup with the field of sharpness in the center of the column is depicted in Figure 1.

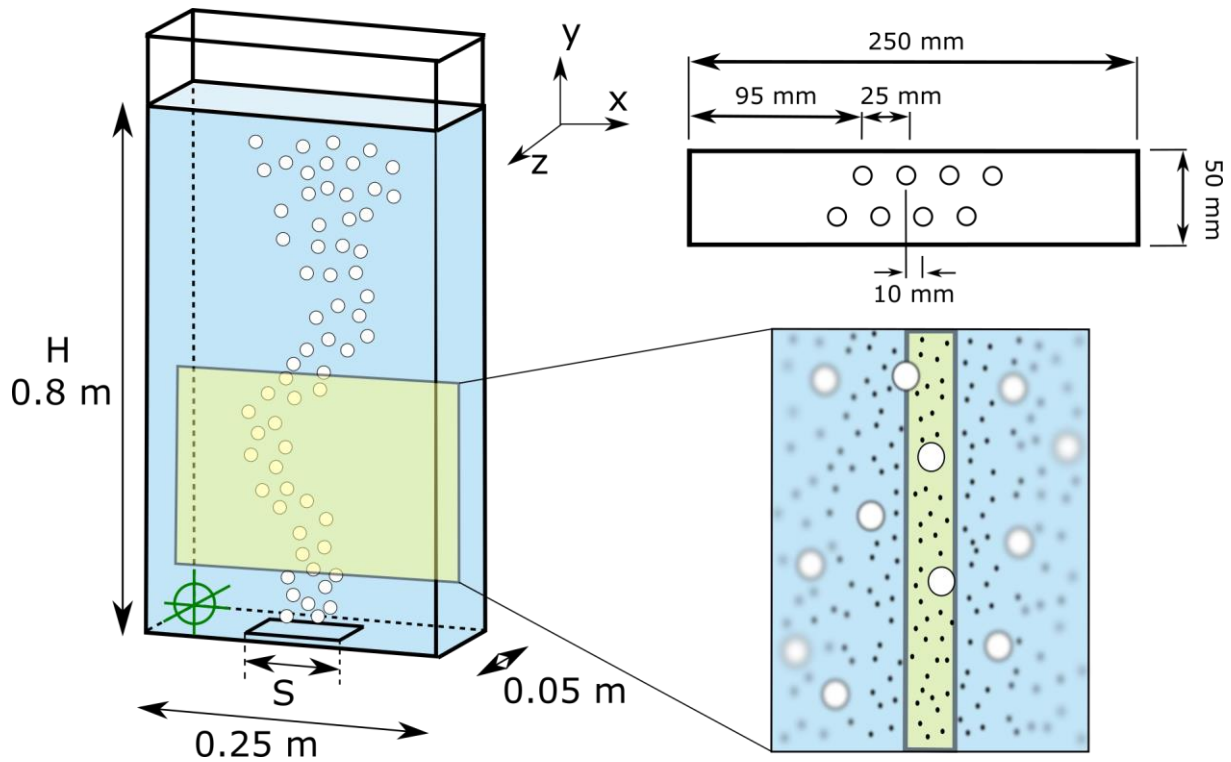


Figure 1: Sketch of the used bubble column (left) with a side view of the field of sharpness with sharp objects in the center and blurred bubbles and particles outside (bottom right) and the ground plate with the positions of the spargers (top right).

For the measurements, 50  $\mu\text{m}$  Polyamide Seeding Particles (PSP) were added to the flow. The setup was backlight illuminated with a 200 W LED. The DOF was adjusted with test particles to a thickness of about 5 mm. Particle images were recorded using a AOS Q-VIT high-speed camera with a 135 mm f2.0 Walimex Pro foto lens.

The image size for PSIV was chosen to be of about 13 cm, which means two measurements per gas flowrate were necessary to cover the complete column width. This image size resulted in a resolution of about 77  $\mu\text{m}/\text{Px}$ . The interrogation area size was 32x32 pixels with 50 % overlap, which corresponds to a size of about 2.5 mm for each cell. A set of eight pictures for the later described multiframe approach were recorded every two seconds. The recordings were taken with a framerate of 2000 fps. Per measurement, the total recording time was 45 minutes.

For PSTV, the same framerate and the same total recording time was chosen. The recordings were also taken every two seconds, but this time just a set of three pictures. The resolution was about two times higher with 30  $\mu\text{m}/\text{Px}$ , which is resulting in a measuring window of 6.3 cm. Therefore, four single measurements were needed to cover the complete column width. In addition, the DOF is therefore only around half the thickness used for the PSIV measurements.

### 3. PSV processing procedures

#### 3.1. PSIV - Image pre-processing

Before the image sequences of the flow can be analyzed with PIV evaluation routines, they undergo several pre-processing steps. Although the light scattering and reflections

of bubble surfaces is strongly reduced with the PSV method, the projected shadow of a bubble would still dominate the correlation step in these areas. Therefore, masking these regions is necessary for every image at first. For this we use a gauss and a median filter to remove tracer particles from the image. Via binarizing the smeared image with a chosen threshold, larger areas belonging to bubbles remain. Afterwards, dilation and erosion steps are applied to exclude brighter regions inside the bubbles. Figure 2 shows an example recording with the corresponding processing steps (a) – (f). Interrogation areas that are colored red belong to the mask. All masked areas will be excluded from further investigations.

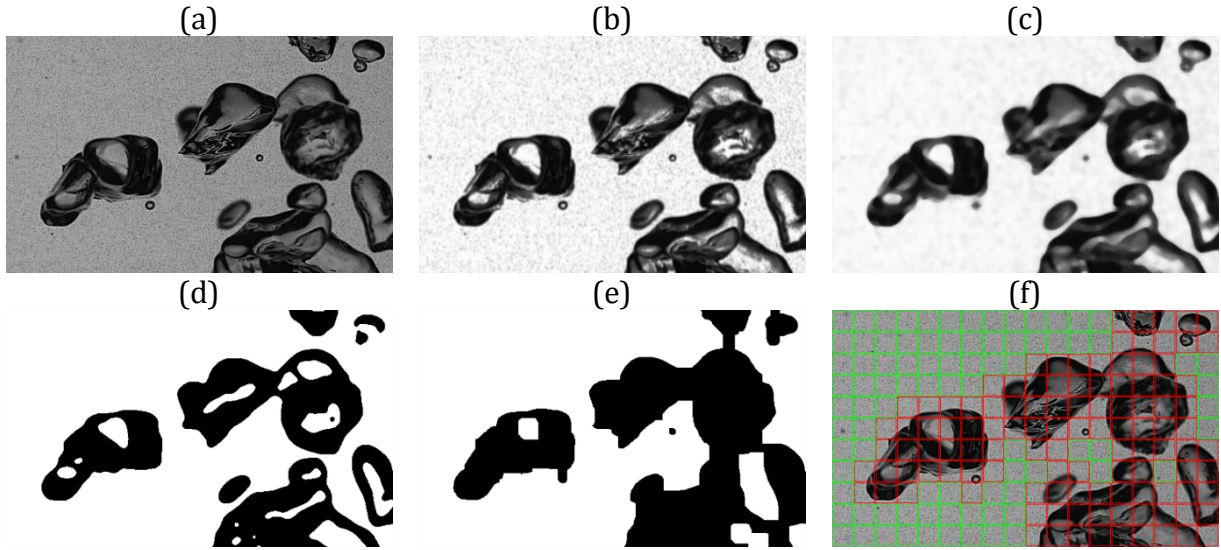


Figure 2: Example of the masking procedure: (a) input image, (b) gauss filter, (c) median filter, (d) binarization, (e) erosion and dilatation, (f) final mask with red areas excluded from further evaluation.

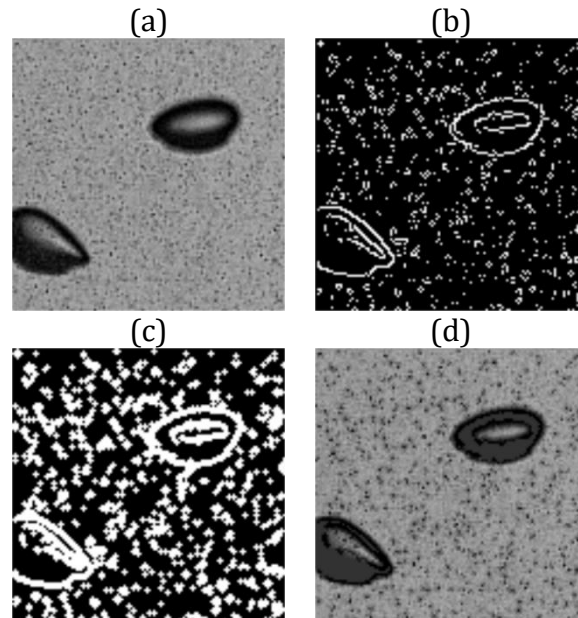


Figure 3: Particle sharpening steps: (a) Laplacian edge enhancement, (b) identified gray value derivatives above the threshold, (c) swelled derivative pixels, (d) contrast enhanced particles.

To improve the PIV correlation step, the influence of out-of-focus tracer particles has to be reduced. In the literature, often thresholds are used to binarize and exclude such particles in the displacement determination (Estevadeordal & Goss, 2005),

(Khodaparast, et al., 2013). The drawback of this method is that shadow intensities close to the threshold can be included in one picture and excluded in the other picture through in-plane movement or small light intensity fluctuations. This increases the probability of spurious vectors determinations. Alternatively, we use a method to increase the influence of sharp particles without erasing slightly blurred particles, which will be described in the following.

The so-called particle sharpening method as an image pre-processing step is shown in Figure 3. At first, an edge enhancement filter with a Laplacian filter function is used to increase the edges of sharp objects. Sharp particles are detected by choosing an appropriate value of the pixel gray value derivatives to their neighborhood. The identified particles and their neighborhood undergo a spreading of the gray value histogram, whereby the contrast of the particles to its surrounding is amplified so that an image with sharpened particles is obtained. Sharpened in this context means that the contrast to the background is enhanced. Consequently, the size of the particle is slightly increased due to the captured neighborhood. With this selectable threshold for the gray value derivatives, the field of sharpness can be additionally manipulated. With a low value, more blurred particles are sharpened so that the thickness of the effective field of sharpness is increased and vice versa.

### 3.2. PSIV - Velocity determination

The complete velocity evaluation procedure is shown in Figure 4 (right side). After pre-processing the pictures and generating the interrogation area grid, the displacements are determined. To calculate the correlation matrix, we use the Fast-Fourier-Transformation (FFT) method

$$\phi = FFT^{-1}(FFT(I_a^*) \cdot FFT(I_b^*)) \quad (1)$$

with

$$I^* = \frac{I - \bar{I}}{cov(I)}. \quad (2)$$

$I(a)$  and  $I(b)$  denote the two gray value intensity distributions at time  $t_0$  and  $t_{0+\Delta t}$ . In comparison to the direct cross-correlation the computational costs for the FFT method are much lower (Raffel, et al., 1998).

Specifically, the determination of instantaneous velocity fields is done in several steps. First, two predictor displacements are determined for every interrogation area. The first predictor  $\Delta X_S$  is determined with a predefined interrogation area size, while the second predictor  $\Delta X_L$  is determined with double the defined pixel size. Using predictors determined with larger interrogation areas is an often-used strategy in PIV evaluation because the number of captured particles is higher and the displacement determination is less sensitive to in-plane loss of particles (Adrian & Westerweel, 2011). The additional use of smaller interrogation areas has the advantage to determine predictors closer to the bubble surfaces without touching masked areas.



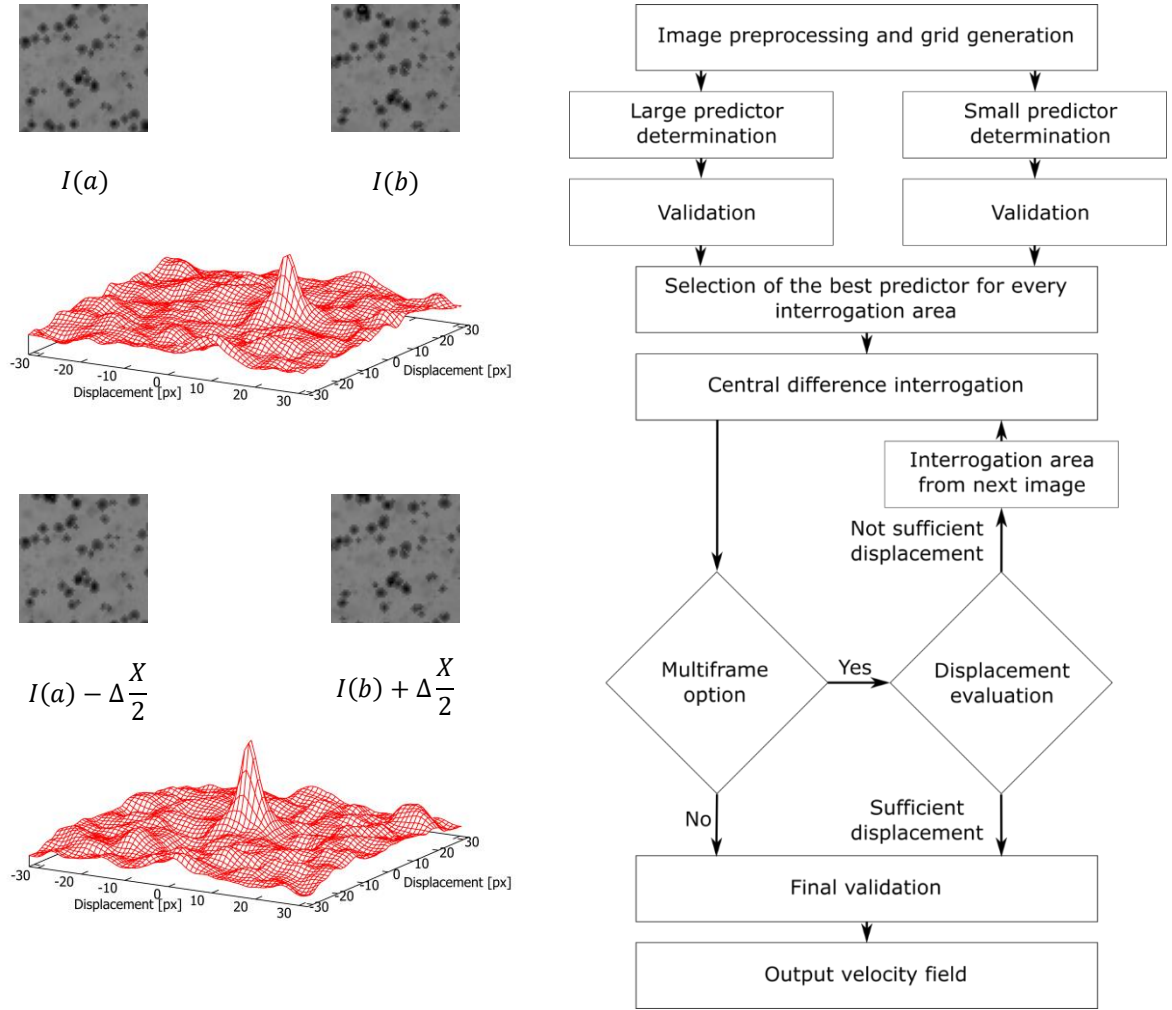


Figure 4: Interrogation areas and corresponding correlation matrix without window offset (top left) and with CDI offset (bottom left); PSIV evaluation steps (right).

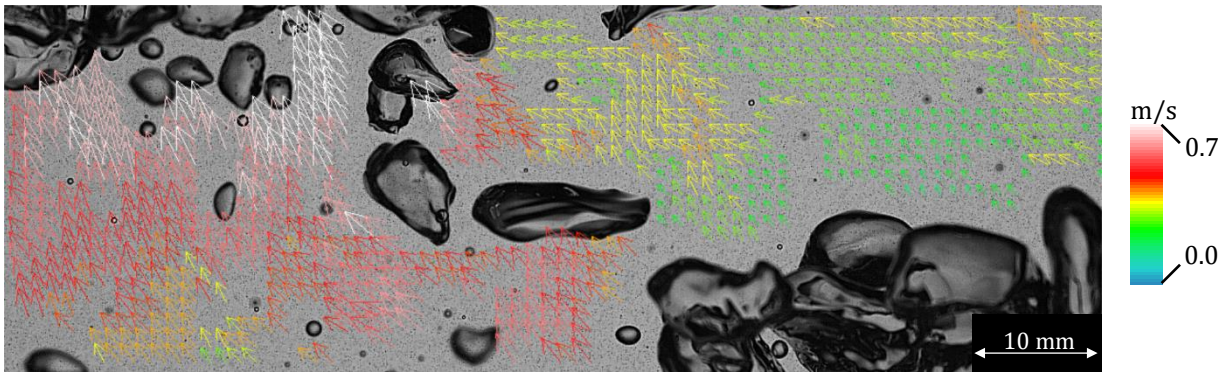


Figure 5: Instantaneous velocity field inside a bubble plume with a gas flow rate of 7 l/min.

After determining the predictors, they are validated using median evaluation of the neighboring velocities as described by Westerweel & Scarano 2005 and the best predictor  $\Delta X$  for every interrogation area is chosen based on the normalized correlation coefficient height. Afterwards, we use a central difference interrogation (CDI) method to shift the interrogation areas, which exhibit second-order accuracy compared to the first-order accuracy forward difference interrogation (FDI) method according to Wereley & Meinhart 2001. The CDI method shifts the interrogation area of the first images  $\Delta \frac{X}{2}$



backward, while the one in the second image is shifted  $\Delta \frac{x}{2}$  forward. The intensity distributions of the new interrogation areas are generated using bilinear interpolation and a new displacement is determined again. Figure 4 (left side) shows an example for a 64x64 pixel interrogation area with the related correlation matrix before the CDI and after the CDI method. For sub-pixel accuracy, we use a three-point Gaussian fit to the detected correlation peak.

For interrogation areas with a smaller predictor  $\Delta X_S$ , the new determined displacement is only added to the predictor if the normalized correlation coefficient height and the ratio to the second highest correlation peak is increased in comparison to the predictor. Therefore, just displacements with a measurable improvement are added to the predictor so that the addition of possible false displacements is avoided.

Interrogation areas with a larger predictor  $\Delta X_L$  are refined to the smaller size before the CDI step and the new determined displacement is always added to the predictor displacement. If the size of these interrogation areas would not be refined, the resulting velocity field would exhibit calculated velocities for different sized interrogation areas.

After determining a velocity field with the previous described steps, we use a so-called multiframe step to increase the accuracy and dynamic range of the velocity measurement (Hain & Kähler, 2007). The determination of small displacement predictors is restricted to the image resolution and the time step between two successive images, which means that discrete displacements smaller than one pixel per time step cannot be captured. Via using pictures with a larger time in between, e.g. the first and the third picture of a sequence, the minimum capturable discrete displacement is decreased and predictors that are more accurate can be determined for small displacements. The multiframe option is applied to all interrogation areas with a displacement below one pixel. In these identified areas, the displacement determination is repeated with the CDI method using later pictures in the recorded sequence. If the displacement is still too small this step is repeated until all areas exhibit a high enough displacement or the last image of a sequence is reached.

Finally, the determined vectors are validated according to their neighborhood again and removed velocities as well as remaining interrogation areas with too small displacements resulting from the multiframe step are interpolated. Since vectors inside high void fraction regions, like in bubble swarms, exhibit only few surrounding velocity information, the distance-weighted eight-point neighborhood is used for validating and interpolating. We chose a validation threshold of two in all measurements as proposed by Westerweel & Scarano 2005. Figure 5 shows an instantaneous velocity field as a result of the described procedure.

### 3.3. PSTV – Particle identification

The particle identification that is needed to track single particles in multiphase flows is not trivial; in particular, if a background illumination with shadowgraphy methods is used instead of a laser illumination. The background of the particles is constantly changing due to the passing bubbles so that a simple threshold or background subtraction is not applicable. From our experience, methods based on the gradients calculated from the grey values are applicable. The background has usually small

gradients so that a simple threshold on the Euclidian norm of the gradient vector field is working well, which is exemplary shown in Figure 6. The problem with this procedure is that the contours of particles are often not closed due to an inhomogeneous illumination. This problem would usually demand a boundary-closing algorithm so that the inside and outside of each particle can be defined. From our experience, such algorithms can cause problems so that we developed a simple shape recognition algorithm.

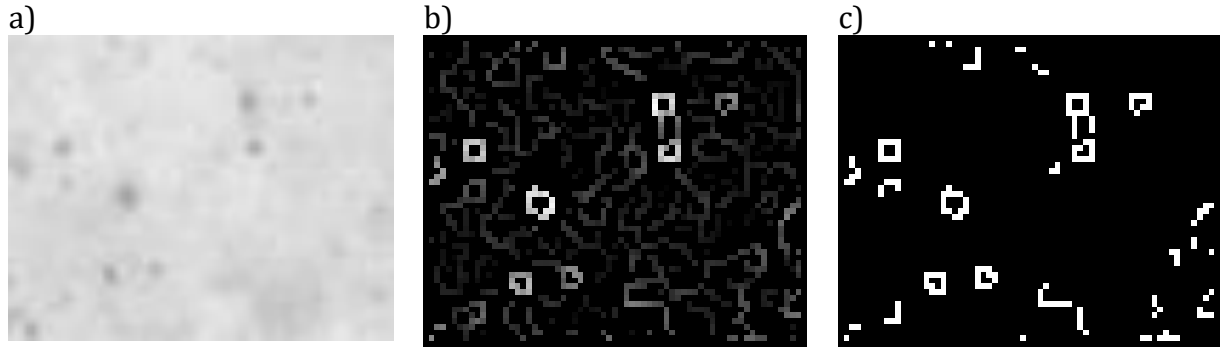


Figure 6 From a typical photograph with 50 $\mu$ m tracer particles (left) the gradient field is calculated with the Sobel operator (middle) on which a threshold is applied (right).

Shape recognition algorithms are widely used, in particular if simple shapes like circles need to be identified. A relatively robust class of algorithms is based on the Hough transformation. The method we developed is inspired by this class but distinctly different since the parameters are not evaluated at the edges but at all other points excluding the edges.

The main problem of identifying small circles is the representation of such on the grid of the optical sensor. This leads to complex shapes, which are irregular and asymmetric as schematically demonstrated in Figure 7. The problem can be handled by imitating the discretization process by evaluating the gradient picture (Figure 6 c) on sub-pixels. For this purpose, an evaluation at the boundaries, in the center, and in the corners was a good compromise between accuracy and computation time.

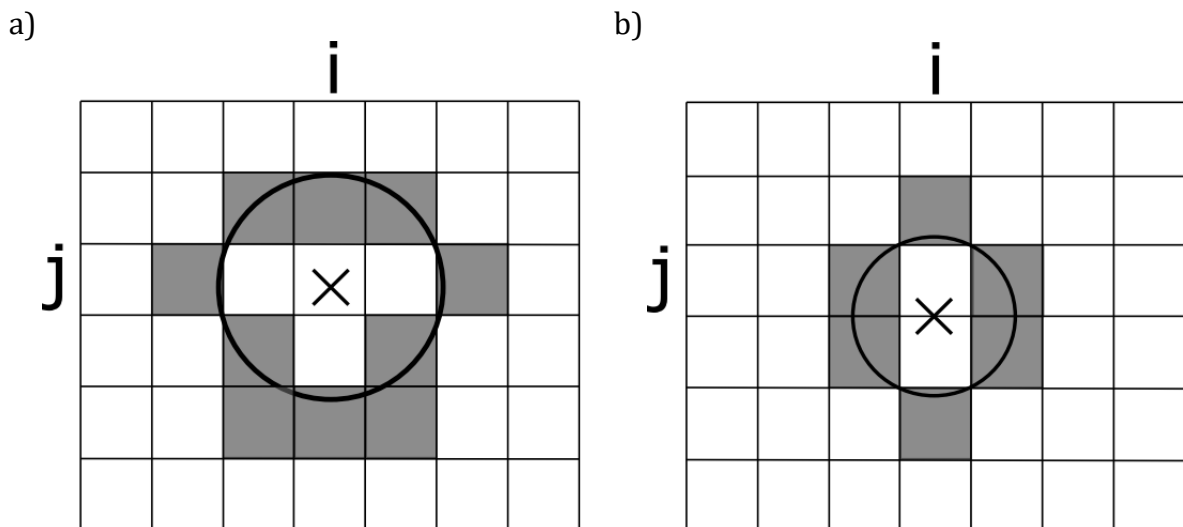


Figure 7 A schematic representation of circles on a grid with the center of the circles marked with crosses.

At each of these nine sub-pixel positions, the distance to the possible edge pixels (Figure 6 c) in an eight pixel large square around the sub-pixel position is calculated. Since a

circle with a specific radius can only have a certain amount of edge pixels, the edge pixels can now be assigned to specific radii. This procedure results in a distribution function, which is shown in Figure 8 for the schematic example from Figure 7. The distribution shown in Figure 8 is obtained at the point closest to the circle center, which is on the center of pixel  $i, j$  (marked in Figure 7) for a) and on the south side of pixel  $i, j$  for b). For the present case, a possible radius of three pixels is sufficient to identify the 50 $\mu$ m particles. The categorization of the edge pixels to the circle radii are given in Table 1. Due to the discrete nature, some circle radii have a larger set than other so that radii with a larger set would be preferred. We tried to account this circumstance by defining a minimum allowed count of edge pixels, which is increasing with increasing circle size. With this side condition, the circle radii from the schematic representation in Figure 7 can be evaluated from Figure 8, which results in 1.75 Px for the a) and 1 Px for b). If two circle radii have the same count of edge pixels and both fulfill the minimum count, the larger radius will be taken.

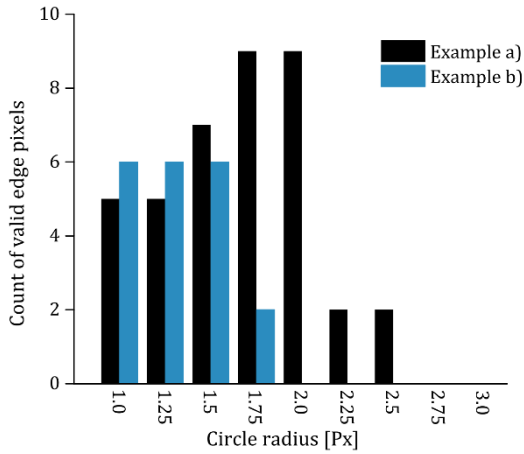


Figure 8 Distribution function obtained from the assignment of the edge pixels to specific circle radii for the examples in Figure 7.

Circle radius [Px]	Set of possible distances [Px <sup>2</sup> ]	Minimal edge pixels
1.0	$1 \leq D^2 \leq 2.25$	6
1.25	$1 \leq D^2 \leq 3.25$	7
1.5	$1.25 \leq D^2 \leq 4.5$	8
1.75	$2 \leq D^2 \leq 5$	9
2.0	$2 \leq D^2 \leq 6.25$	10
2.25	$5 \leq D^2 \leq 8.5$	12
2.5	$5 \leq D^2 \leq 10.25$	14
2.75	$8 \leq D^2 \leq 12.25$	16
3	$8 \leq D^2 \leq 13$	18

Table 1 Classification of the circle size depending on the distance, D, to the edge pixels.

This procedure of determining the circle size is executed for every sub-pixel and pixel positions. This leads to the parameter space that is exemplary shown in Figure 9 for the example given in Figure 6. The side condition of a minimum count of edge particles can now be used to filter the parameter space in order to simplify the finding of the local maxima (Figure 9 right).

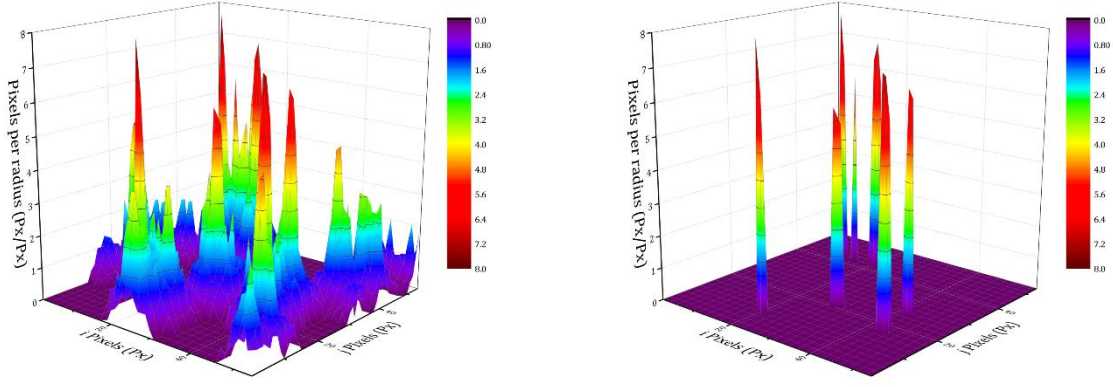


Figure 9 The parameter space obtained by applying the transformation for the example given in Figure 6 (left) and the result when the side condition of minimal allowable edge pixels is applied (right).

In order to reduce the computation time, pixels are pre-selected with an adaptive threshold (Figure 10). The result of the particle identification for the example in Figure 6 is shown in Figure 10. To increase the sub-pixel accuracy, the pixels inside the found circles are fitted to a two-dimensional Gaussian function

$$f(x, y) = A \exp \left[ -\frac{(x - x_0)^2}{2\omega_x} - \frac{(y - y_0)^2}{2\omega_y} \right] + \epsilon_{xy} \quad (3)$$

Which can be linearized to

$$\ln(I_{xy}) = a_1 x^2 + a_2 x + a_3 y^2 + a_4 y + a_5 \quad (4)$$

In the linear equation  $x$  and  $y$  are the relative coordinates of the pixels inside the circle to the circle center. Every pixel delivers one equation so that the resulting system of linear equations can be solved easily. The center of tracer particle is calculated by  $x_0 = -0.5 \frac{a_2}{a_1}$  and  $y_0 = -0.5 \frac{a_4}{a_3}$ .

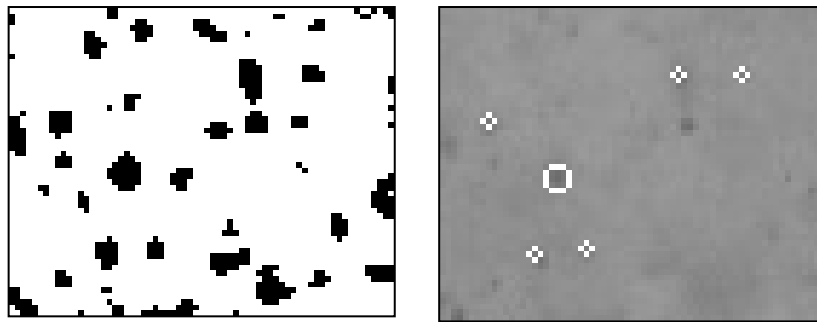


Figure 10 Pre-selected pixels used the transformation are colored black (left) and the final result (right).

### 3.4. PSTV - Particle Tracking

For tracking the identified particles, we use a brute force algorithm with a correction step. The basic idea of the algorithm is to find patterns of tracer particles in the subsequent image. For this purpose, sets of tracer particles in the two subsequent images are compared. To do this, a distance function of two sets of tracer particles is defined. The two sets with the lowest distance are treated as similar; the shift of these two sets in the subsequent images is used to calculate the velocity.

The first step is to find the neighbors,  $N$ , around a specific tracer,  $T_a$ , which is simply done with a distance function that is limited by a radius  $R$

$$N_t = \{T \in \text{Tracer in image } t \mid |T_a - T| < R_t\} . \quad (5)$$

The second step is to find the possible tracer in the next image, which is realized with the same distance function

$$N_{t+1} = \{T \in \text{Tracer in image } t + 1 \mid |T_a - T| < R_{t+1}\} . \quad (6)$$

For the brute force loop, the tracers in  $N_t$  are now shifted pixel-wise around. When a tracer,  $T$ , has the position  $(i_T, j_T)$ , this can be written as

$$N_{t,kl} = \{(i_T + k, j_T + l), T \in N_t \mid \|(k, l)\| < R_v\} . \quad (7)$$

The shift of  $k$  pixels in the  $i$  direction and  $l$  pixels in the  $j$  direction of the tracers  $T$  from the neighborhood  $N_t$  is limited by the radius  $R_v$ , which is equal to a maximal allowed velocity.

Now, the distance between the set of tracer particles in  $N_{t,kl}$  and  $N_{t+1}$  is evaluated; the likely displacement vector of  $T_a$  is at the lowest distance with the velocity components  $k$  and  $l$ . The distance of  $N_{t,kl}$  and  $N_{t+1}$  is here defined as the sum of the Euclidean distance of a tracer in  $N_{t,kl}$  and its nearest tracer in  $N_{t+1}$ . So that in a first step, the nearest tracer for every tracer in  $N_{t,kl}$  is searched in  $N_{t+1}$ , which can be written as a set of tracer pairs

$$S_{kl} = \{(T_{t,kl}, T_{t+1}) \mid T_{t,kl} \in N_{t,kl}, T_{t+1} \in N_{t+1} \wedge \text{nearest to } T_{t,kl}\} . \quad (8)$$

The distance between tracer pairs in  $S_{kl}$  is now summed up, which is the distance between  $N_{t,kl}$  and  $N_{t+1}$ .

$$\|(N_{t,kl}, N_{t+1})\| := \sum_{\forall (T_{t,kl}, T_{t+1}) \in S_{kl}} \|(T_{t,kl}, T_{t+1})\| . \quad (9)$$

A normalization is not necessary since the cardinality of all  $S_{kl}$  is always the same.  $\|(T_{t,kl}, T_{t+1})\|$  is the Euclidian norm to calculate the distance between two tracers

$$\|(T_{t,kl}, T_{t+1})\| := |(i_{T_{t+1}} - i_{T_{t,kl}}, j_{T_{t+1}} - j_{T_{t,kl}})| . \quad (10)$$

Now, we obtain for every allowed displacement  $(k, l)$  a distance, the likely displacement vector is defined at the smallest distance. If two or more displacements have the same distance, the smallest displacement will be taken. To apply subpixel accuracy, the velocity vector is calculated by using the position of the tracer  $T_a$  and the tracer in  $N_{t+1}$  that is closest to the displaced tracer  $T_{a,kl}$ .

In bubbly flows, usually a strong velocity component perpendicular to the measuring plane is present. Therefore, many tracer particles travel outside the observation area between two images. The resulting change of tracer patterns is causing spurious vectors.

An identification of outliers by the standard deviation of the entire set of vectors is not useful since the outliers cause an overestimation of the standard deviation. Therefore, we search a representative set of vectors with which the standard deviation can be calculated. At a first step, we search again the neighborhood around tracer  $T_a$ , which is illustrated in Figure 11 a) for a test case.

$$N_o = \{T \in \text{Tracer in image } t \mid |T_a - T| < R_o \} . \quad (11)$$

The velocities inside this neighborhood are now transferred on a discretized velocity map (Figure 11 b)) and the count inside the discretized cells is determined (Figure 11 c)). The vectors inside the cell with the largest count are now used to calculate an averaged vector  $\vec{v}_{AVG}$  and standard deviation  $\sigma$  with which spurious vectors are identified. The spurious vectors are reiterated with the algorithm explained by Eq. (5) - (10), but with a restriction for  $N_{t+1}$  in Eq. (6). We implement the restriction in a way that only vectors are allowed that would fulfill the following condition

$$|\vec{v} - \vec{v}_{AVG}| < c \cdot \sigma . \quad (12)$$

However, in the present work, the concrete implementation of the correction step differs from the illustration in Figure 11 b) and c). At first, we use not a rectangular discretization but a circular one. Second, the discretization is overlapping so that the drawbacks of a discretized velocity map are attenuated. Further, to overcome the drawback of fixed positions for the discretization, the average velocity of the cell with the largest count is calculated, the center of an additional cell is shifted on this velocity. When this additional cell has a larger count than the previous largest cell, this additional cell is used to calculate  $\vec{v}_{AVG}$  and  $\sigma$ . The constants for the present setup are chosen as follows:  $R_o = R_t = R_{t+1} = R_v = 1.5 \text{ m/s}$ , the count of the discretization cells  $= \frac{R_o}{7}$ , the size of the cells  $= \frac{R_o}{5}$ , and  $c = 3.5$ .



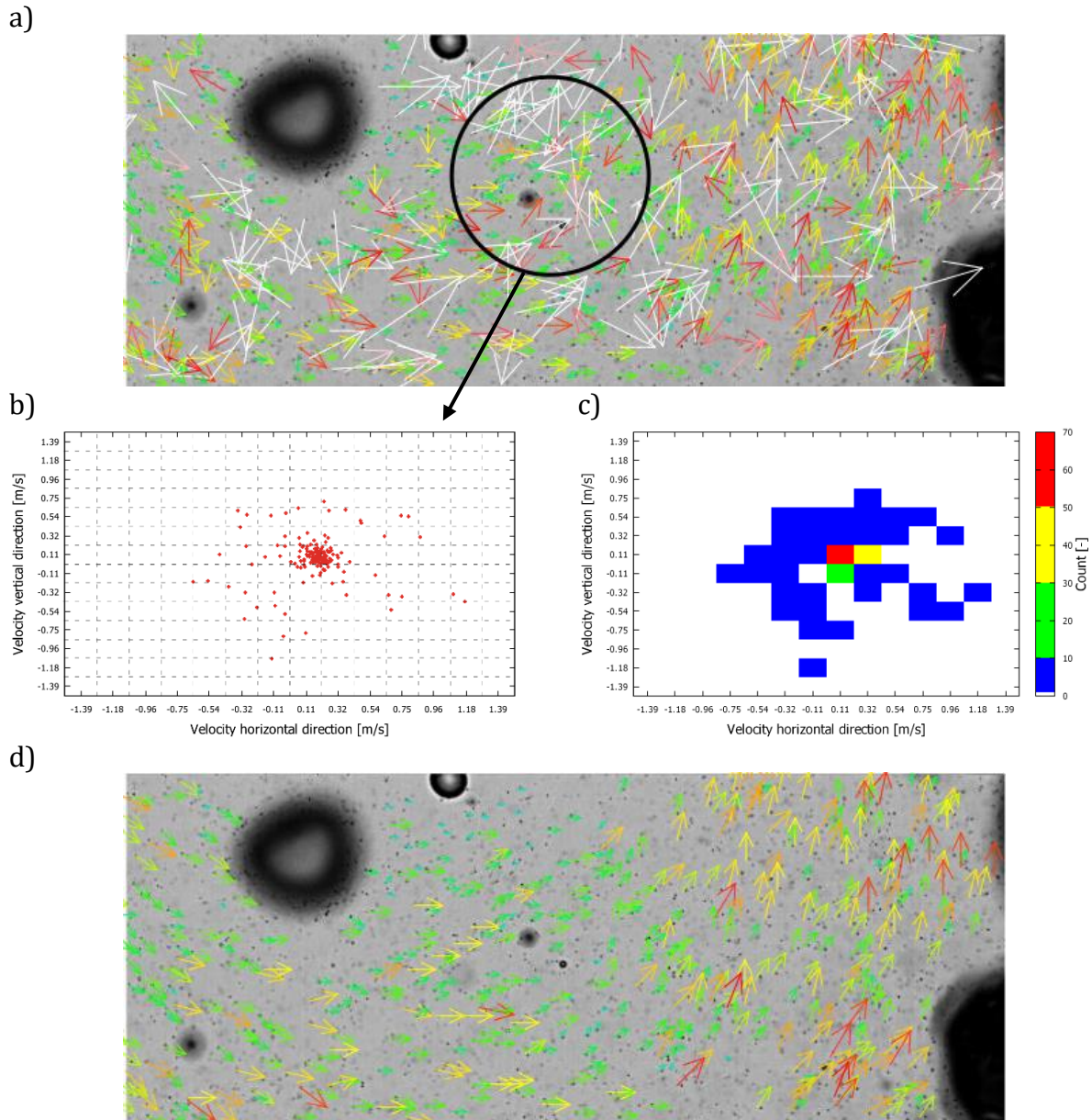


Figure 11 Identification and correction of spurious vectors for a test case: a) Identification of the neighborhood around a specific vector, b) transferring the velocities in the neighborhood to a discretized velocity map, c) count of the vectors inside the grid cells of the velocity map, d) result after reiteration.

A result of the PTSV algorithm is shown in Figure 12. Compared to PSIV, the resolution is higher so that smaller scales can be seen. In addition, velocities closer to the bubbles can be recorded since no interrogation areas are used.

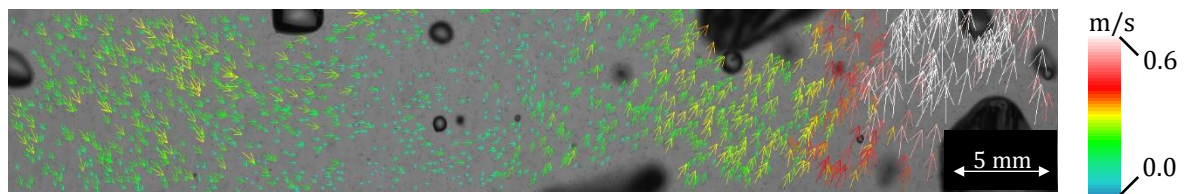


Figure 12 Result of the PTSV algorithm at 5 l/min gas volume flow rate.

### 3.5. Sampling bias

Due to the blocking bubbles, the local amount of velocity information is changed and a statistical tool for correct averaging in time and space is necessary. Ziegenhein & Lucas 2016 showed that a simple ensemble averaging leads to a sampling bias. To overcome

this problem, they introduced a so-called hold processor for evaluating PIV data in bubbly flows. At first, a grid of a chosen cell size is defined. The hold processor collects all velocity information in an instantaneous velocity field and allocates them to their corresponding grid cell. If a cell exhibits no velocity, the hold processor waits in time. The velocities in the other cells are collected in the meantime. This is repeated until every grid cell is filled with at least one vector. Afterwards the velocities are averaged and a normalized instantaneous velocity field is obtained. If this hold processor is not used, higher velocities would be underweighted in regions with higher void fraction since the amount of vectors is connected to the gas phase, which induces higher velocities due to buoyancy. The hold processor is applicable on the PSIV as well as the PSTV method. For the PSIV method all velocities in interrogation areas that are located inside a grid cell are collected and allocated to the cell. The same is done with identified particle velocities of the PSTV method. For more information, the reader is referred to Ziegenhein & Lucas 2016.

## 4. Results

---

### 4.1. Comparison ensemble average versus hold processor

In the following section, the influence of the hold processor for the tested bubble plume configurations is shown. The measuring area is therefore divided in 24 horizontally equal sized grid cells for both averaging procedures. Figure 13 shows the resulting profiles for the vertical velocity component evaluated with the PSIV procedure. Clearly, higher velocities are underweighted in the center region with an ensemble average. This effect increases with increasing flow rate since the void fraction and therefore the number of masked regions increases, while at the same time the liquid is stronger accelerated in the center due to the higher void fraction. At higher gas flowrates, the hold processor becomes significant at the wall, too. The recirculation vortexes become stronger with higher flowrates and start transporting bubbles downstream. In this situation, the negative vertical velocities are underestimated with an ensemble averaging, since a higher void fraction, and therefore more masked bubbles, is correlated to a higher negative velocity.

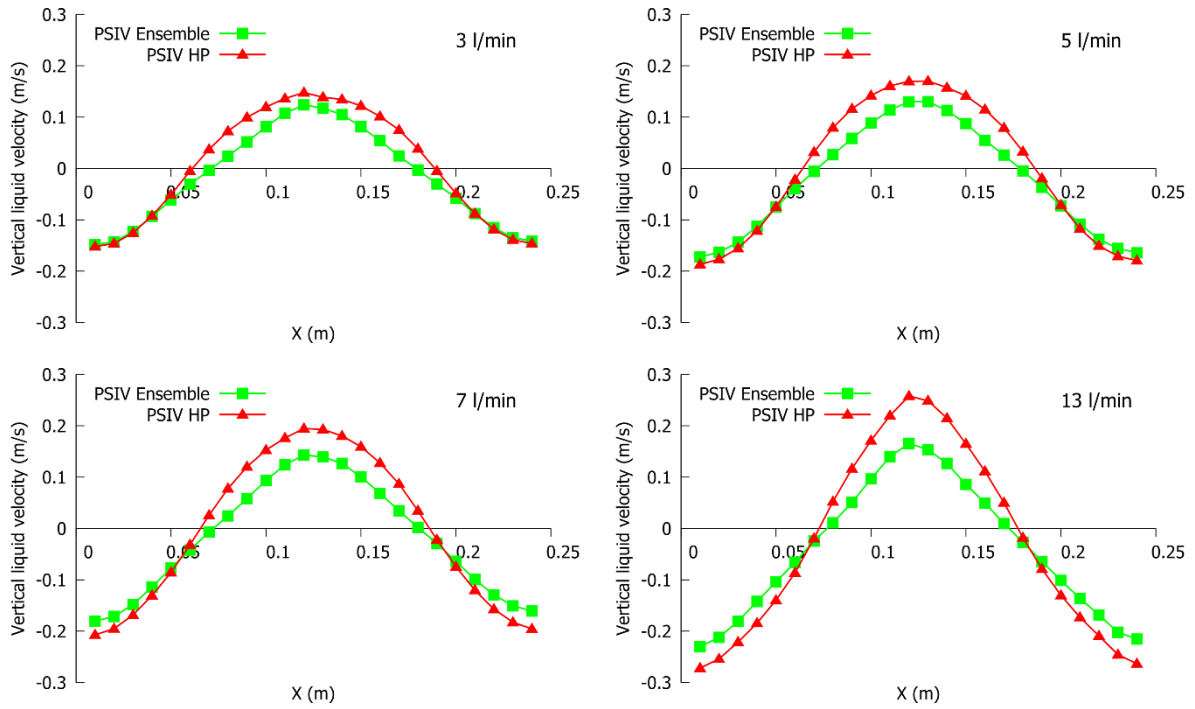
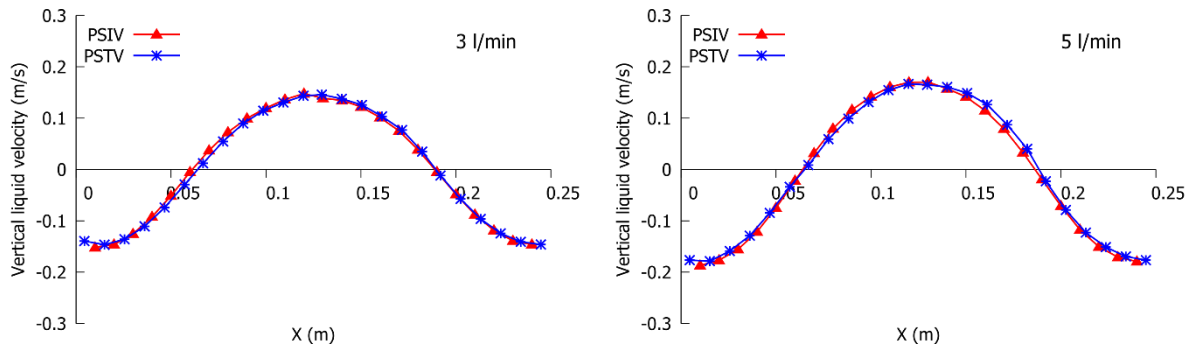


Figure 13: Vertical liquid velocity component of ensemble averaging and averaging with the hold processor with the PSIV method.

#### 4.2. Comparison PSIV versus PSTV

Since the significance of the hold processor was demonstrated in section 4.1, results for PSIV and PSTV are discussed with the hold processor in the following. Figure 14 shows the comparison for the upward liquid velocity. For lower flowrates up to 7 l/min, both methods show a good agreement across the column width. Only the case with a gas flowrate of 13 l/min exhibits small differences across the profile. An explanation for this could be that PSTV is able to capture higher upwards velocities closer to the bubble surfaces, which are missed due to the masked regions in the PSIV method.



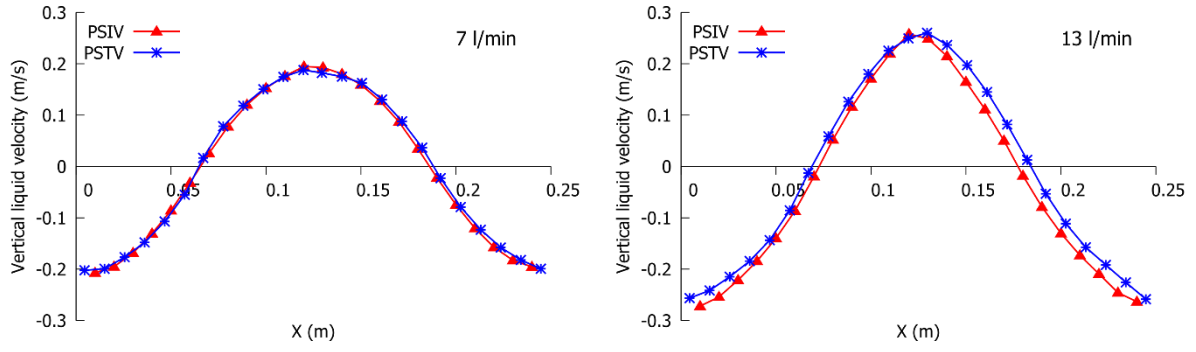


Figure 14: Vertical liquid velocity component of the PSIV and PSTV methods.

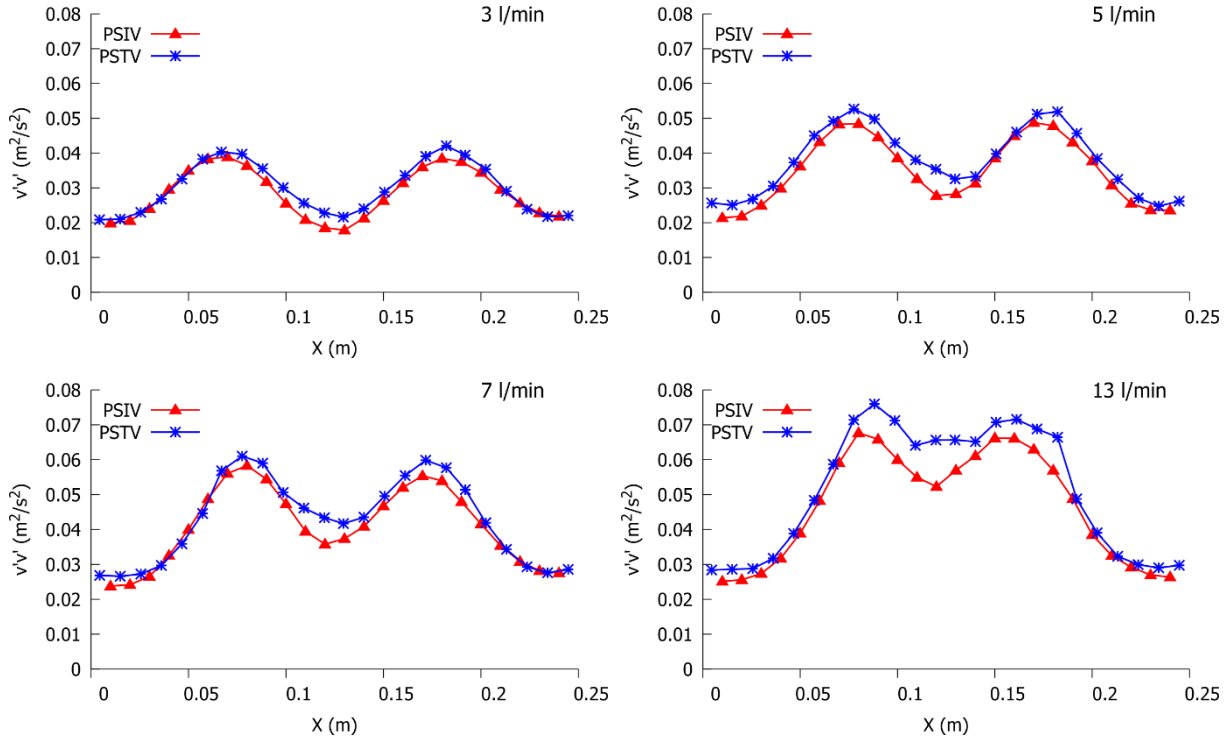


Figure 15: Upward Reynold stress component of the PSIV and the PSTV methods.

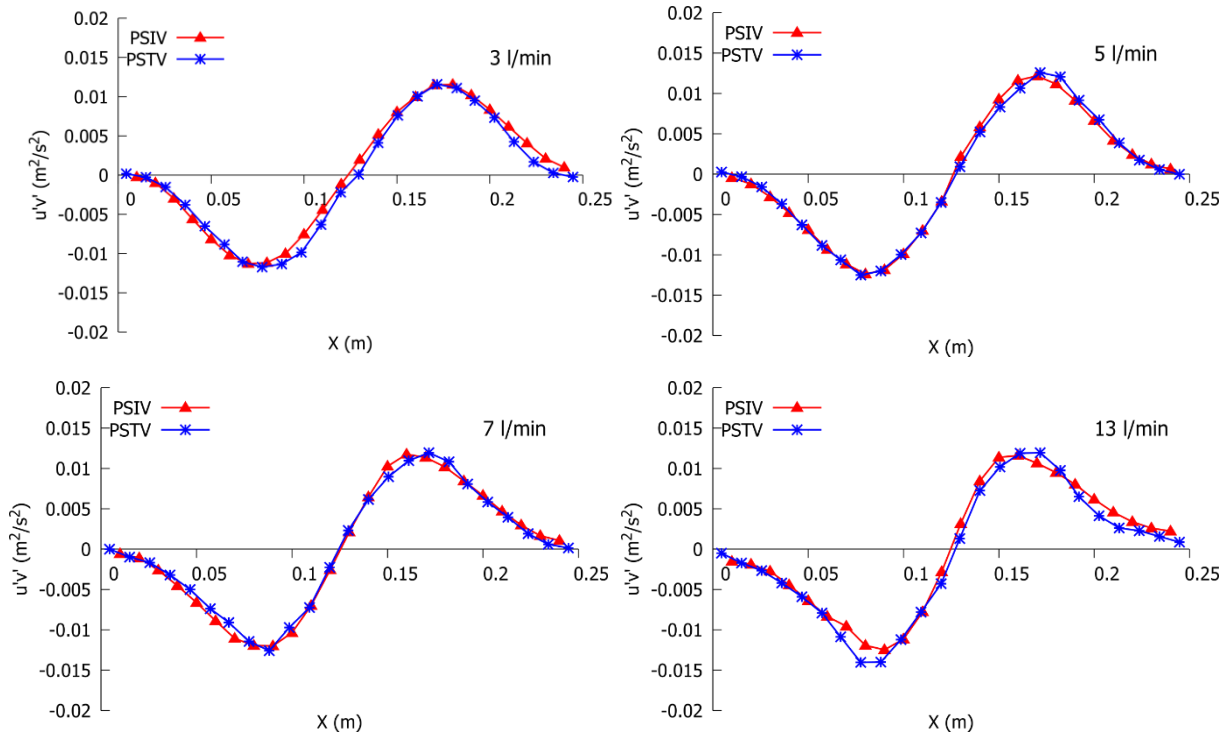


Figure 16: Cross Reynold stress component of the PSIV and the PSTV methods.

As Ziegenhein & Lucas 2016 demonstrated, not only velocity information but also the Reynolds stresses have to be treated with the hold processor. Therefore, all following results for the normal Reynolds stress component  $v'v'$  and the cross Reynolds stress component  $u'v'$  are obtained using the hold processor. Figure 15 shows the upward Reynold stress component along the column width. Both methods show the highest values in the regions next to the center as usually observed in bubble plumes (Mudde, et al., 1997). Clearly, the PSTV method shows slightly higher values due to higher spatial resolution and the box filter of the PSIV method due to the defined interrogation area size.

For the cross Reynold stress component shown in Figure 16 only small differences can be observed. Again, these differences are the highest for the highest flowrate. The results show central symmetry and are a magnitude lower than the normal Reynolds stress, which is in agreement with other results reported in the literature (Mudde, et al., 1997), (Yang, et al., 1993).

## 5. Conclusion

Particle Shadow Velocimetry (PSV) with volume illumination and a small depth of field (DOF) was used to evaluate liquid velocities of an oscillating bubble plume inside a rectangular bubble column. Particles in a thin field of sharpness were used to determine velocity fields in the center of the column. The avoidance of a usually used laser-sheet coming from the side prevented strong light scattering at the bubble surfaces and lateral bubble shadows covering the tracer particles.

Two different evaluation procedures were described to determine the particle displacements from consecutively recorded images of a bubbly flow that is seeded with

50 $\mu$ m tracer particles. The Particle Shadow Image Velocimetry (PSIV) procedure is based on standard PIV processing steps as well as additional image processing steps. These additional steps include a bubble mask to exclude bubble shadows from the liquid velocity investigation and a so-called particle sharpening step. The latter can be used to manipulate the thickness of the sharpness field.

Moreover, a Particle Shadow Tracking Velocimetry (PSTV) procedure was described, which enables the tracking of single particle shadows in high particle image densities. The particle identification is realized by a transformation similar to the Hugh transformation. This transformation performed well for particles that are represented with a 1-3 pixel radius. The particle-tracking algorithm is based on the identification of similar patterns of tracer particles. Thereby the distance function that is used to define if a pattern is similar to another pattern can be easily adjusted. We observed that in bubbly flows the out of plane motion could be very strong so that spurious vectors occur. The identification of these vectors was realized with the standard deviation of variable vector sets; the identified spurious vectors were afterward reiterated.

The results of velocity and some shown turbulence parameters from both procedures coincide for almost all gas flowrates. With increasing flowrate, however, minor differences occur between both procedures. A reason could be the different spatial resolution used for PSIV and PSTV.

Summarizing, liquid velocity measurements in bubbly flows with gas fractions over 10% are quite difficult. Many bubbles passing the field of interest generate inhomogeneous velocity gradients and block the measurement irregularly. The most difficult part is a proper illumination of the tracer particles inside bubble swarms and close to a bubble surface. A backlight illumination performed very well compared to a laser-sheet illumination from the side (Ziegenhein & Lucas, 2016). Disturbing reflections on the surface are avoided so that measurements very close to the surface are possible. Moreover, the influence of shadows is reduced since the column can be illuminated through the thinner depth coordinate. This benefit might be repealed in round columns. However, the experimental setup is greatly simplified with a backlight; in particular, a LED can be used without safety measures so that field measurements outside laser labs are possible. The most important benefit of the backlight illumination is the fixed depth of field. A laser-sheet scatters on the interfaces, which results in an illumination of tracers behind and before the intended laser sheet so that no defined measurement volume is given. The good agreement of both developed procedures indicate validity of the results and thus the PSV method can be designated as promising to become a standard method for further velocity measurements in bubbly flows.



## References

---

- Adrian, R. J. & Westerweel, J., 2011. *Particle Image Velocimetry*. s.l.:Cambridge University Press.
- Bröder, D. & Sommerfeld, M., 2007. Planar shadow image velocimetry for the analysis of the hydrodynamics in bubbly flows. *Meas. Sci. Technol.*, Volume 18, pp. 2513-2528.
- Brücker, C., 2000. PIV in two-phase flows. *Lecture Series 2000-01 Particle Image Velocimetry and associated techniques*.
- Estevadeordal, J. & Goss, L., 2005. *PIV with LED: Particle Shadow Velocimetry (PSV)*. Reno, Nevada, 43rd AIAA Aerospace Sciences Meeting and Exhibit.
- Hain, R. & Kähler, C. J., 2007. Fundamentals of multiframe particle image velocimetry (PIV). *Exp Fluids*, Volume 42, pp. 575-587.
- Khodaparast, S., Borhani, N., Tagliabue, G. & Thome, J. R., 2013. A micro particle shadow velocimetry ( $\mu$ PSV) technique to measure flows in microchannels. *Exp Fluids*, Volume 54.
- Khodaparast, S., Borhani, N. & Thome, J. R., 2014. Application of micro particle shadow velocimetry  $\mu$ PSV to two-phase flows in microchannels. *International Journal of Multiphase Flow*, Volume 62, pp. 123-133.
- Marxen, M., Sullivan, P. E., Loewen, M. R. & Jähne, B., 2000. Comparison of Gaussian particle center estimators and the achievable measurement density for particle tracking velocimetry. *Experiments in Fluids*, Volume 29, pp. 145-153.
- Meinhart, C. D., Wereley, S. T. & Gray, M. H. B., 2000. Volume illumination for two-dimensional particle image velocimetry. *Meas. Sci. Technol.*, Volume 11, pp. 809-814.
- Mudde, R. F., Lee, D. J. & Fan, L.-S., 1997. Role of coherent structures on reynolds stresses in a 2-D bubble column. *A.I.Ch.E. Journal*, Volume 43, pp. 913-926.
- Murai, Y., Oishi, Y., Takeda, Y. & Yamamoto, F., 2006. Turbulent shear stress profiles in a bubbly channel flow assessed by particle tracking velocimetry. *Experiments in Fluids*, Volume 41, pp. 343-352.
- Raffel, M., Willert, C. & Kompenhans, J., 1998. *Particle Image Velocimetry - A Practical Guide*. s.l.:Springer-Verlag.
- Santiago, J. G. et al., 1998. A particle image velocimetry system for microfluidics. *Experiments in Fluids*, Volume 25, pp. 316-319.
- Wereley, S. T. & Meinhart, C. D., 2001. Second-order accurate particle image velocimetry. *Experiments in Fluids*, Volume 31, pp. 258-268.
- Wereley, S. T. & Meinhart, C. D., 2010. Recent Advances in Micro-Particle Image Velocimetry. *Annu. Rev. Fluid Mech.*, Volume 42, pp. 557-576.
- Westerweel, J., 1997. Fundamentals of digital particle image velocimetry. *Meas. Sci. Technol.*, Volume 8, pp. 1379-1392.

Westerweel, J. & Scarano, F., 2005. Universal outlier detection for PIV data. *Experiments in Fluids*, Volume 39, pp. 1096-1100.

Yang, Y. B., Devanathan, N. & Dudukovic, M. P., 1993. Liquid backmixing in bubble columns via computer-automated radioactive particle tracking (CARPT). *Experiments in Fluids*, Volume 16, pp. 1-9.

Ziegenhein, T., Garcon, M. & Lucas, D., 2016. Particle tracking using micro bubbles in bubbly flows. *Chem. Eng. Sci.*

Ziegenhein, T. & Lucas, D., 2016. On sampling bias in multiphase flows: Particle image velocimetry in bubbly flows. *Flow Measurement and Instrumentation*, Volume 48, pp. 36-41.